Effect of molecular ordering on spin and charge injection in rubrene

Citation: Raman, K. V. et al. "Effect of molecular ordering on spin and charge injection in rubrene." Physical Review B 80.19 (2009): 195212. © 2009 The American Physical Society

As Published: http://dx.doi.org/10.1103/PhysRevB.80.195212

Publisher: American Physical Society

Persistent URL: http://hdl.handle.net/1721.1/52587

Version: Final published version: final published article, as it appeared in a journal, conference proceedings, or other formally published context

Effect of molecular ordering on spin and charge injection in rubrene

K. V. Raman,[1,*] S. M. Watson,[2] J. H. Shim,[1] J. A. Borchers,[2] J. Chang,[1,3] and J. S. Moodera[1]
[1]*Francis Bitter Magnet Laboratory, MIT, Cambridge, Massachusetts 02139, USA*
[2]*National Institute of Standards and Technology, Gaithersburg, Maryland 20899, USA*
[3]*Center for Spintronics Research, Korea Institute of Science and Technology, Seoul, Korea*
(Received 30 July 2009; revised manuscript received 29 October 2009; published 30 November 2009)

Studies have shown that interfaces play a crucial role for efficient spin injection and transport. Here, we address the complex role of interface in spin and charge injection into organic materials by various interface-sensitive characterization tools. Inelastic tunneling spectroscopy and polarized neutron reflectometry were mainly adopted to explore the interfaces of high mobility organic semiconductor rubrene sandwiched by two ferromagnetic electrodes. The dramatic difference in the reported magnetotransport properties and charge injection characteristics in trilayer magnetic junctions has been attributed to the different growth morphology of rubrene molecules at the interface dictated by the presence or absence of a 0.6 nm alumina seed layer. The magnetic contribution of the top ferromagnetic electrode is also influenced by the morphology of the rubrene layer underneath, directly affecting the spin injection efficiency. This work highlights the importance of interface engineering in the development of organic-based spintronics devices.

DOI: 10.1103/PhysRevB.80.195212 PACS number(s): 72.25.Dc, 72.25.Mk, 72.80.Le, 75.47.−m

Spin transport in π-conjugated organic semiconductors (OSs) is necessarily a vast and complex area that is just beginning to be explored.[1] Recent demonstrations of spin transport in organic materials[2–6] have been promising, giving impetus to explore the potential of OSs in spintronics applications. Although their study can be extremely challenging, it is expected to be rich in knowledge. For instance, unlike inorganic semiconductors, OSs have shown significantly complex charge injection and transport mechanisms. To date, several theories have dealt with the transport phenomena: modeling the strong electron-phonon coupling (polarons) and the structural disorder of the molecules to account for the observed transport characteristics in different organic systems.[7–9] Growth-related structural changes in OS films have also been known to influence the transport properties[10] and, consequently, the spin injection and transport, as observed in this work. Due to the complexity associated with organic systems, appropriate characterization methods need to be implemented to understand the spin transport.

In our recent work, we demonstrated a large tunneling magnetoresistance (TMR) of 6% at room temperature, showing a spin-diffusion length of 13 nm in thin amorphous rubrene films ($C_{42}H_{28}$).[11] The study was performed in the tunnel junction structure for hybrid (rubrene film grown on alumina as tunnel barrier) and rubrene (rubrene film grown without alumina seed layer) barriers. In this work, we address the role of interfaces, their influence on the growth morphology of the OS, and hence on the transport properties by performing interface-sensitive characterization by inelastic tunneling spectroscopy (IETS) and polarized neutron reflectometry (PNR) measurements. Charge and spin transport measurements were extended to thick rubrene barriers (>20 nm) to obtain information on the evolution of the film morphology with thickness in both types of junctions.

Samples for IETS measurements were prepared as a metal-insulator-metal structure with a thin rubrene barrier film to form hybrid junctions (HJs) and rubrene junctions (RJs). The layers were all grown *in situ* using a shadow mask technique[3,11] in a deposition chamber with a base pressure of 6×10^{-8} Torr. In the case of HJs, the bottom electrode and a thin Al layer (0.5 nm) were grown at low temperature (80 K). This was followed by short (6–8 s) oxygen plasma exposure (500 W at 60 mTorr) to form a thin alumina seed layer. The rubrene barrier and the top electrode were then deposited at room temperature to form the junction (200×200 μm^2).

IETS is a powerful tool to analyze the active vibrational modes of molecules within the barrier, in probing their orientation, structural, electronic, and chemical modifications.[12,13] The strong electron-phonon coupling in organic materials makes IETS a highly interface-sensitive characterization tool compared to other spectroscopic methods such as Raman and infrared (IR). Unlike Raman and IR spectroscopy, the wavelength of the probing tool (electrons) in IETS is much smaller. As a result, the selection rules, governing the symmetry of the vibrating dipoles with respect to the probing wavelength, are different in IETS and depend only on the orientation of the molecules as predicted and observed experimentally.[13]

IETS was carried out at 4.2 K using a lock-in technique, with an ac modulation of 5 mV at 495 Hz to improve the signal detection. Figure 1 shows the IETS results ($\frac{d^2I}{dV^2}$ *vs* V) for the HJ and the RJ. All the major peaks in the IETS plot were carefully examined for reproducibility. The computed Raman and IR spectroscopy peaks with relative intensities for single-crystal rubrene by Weinberg-Wolf *et al.*[14] are also shown in Fig. 1. The IETS data were also obtained for control junctions with only Al_2O_3 barrier (no rubrene) to identify the peaks due to rubrene molecules in the barrier. The Al-phonon mode at ~33 mV (Ref. 15) and the Al-O stretching modes at ~107 mV (Ref. 16) are identified. For the HJ, the peak position and the relative intensity of the different active phonon modes are found to match well with the Raman and IR peaks obtained for the free standing rubrene single crystals, showing that the rubrene molecules are *not structurally altered* in the *barrier* of *our junctions*. However, for the RJ, strong low-energy modes with additional trap-assisted reso-

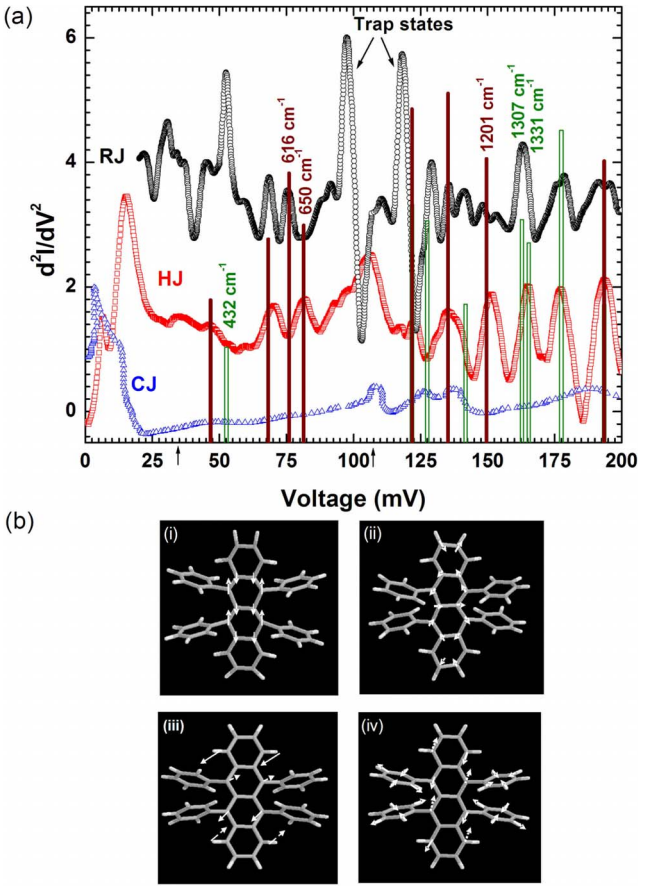

FIG. 1. (Color online) (a) IETS plots of RJ [Al(8)/Rub(10)/Al(10)] (circle) and HJ [$Al(8)/Al_2O_3(0.6)/Rub(6)/Al(10)$] (square) with IETS plot of control junction (CJ) [$Al(8)/Al_2O_3(1)/Al(8)$] (triangles), and computed Raman (solid bar) and IR (hollow bar) peaks for single-crystal rubrene included for reference (all thicknesses are in nm). The IETS plots are shifted vertically for clarity. The arrows on the *x*-axis correspond to the position of Al phonon mode (~33 mV) and Al-O stretching mode (~107 mV), (b) Active molecular vibrational modes observed in hybrid junctions at (i) 1201 cm^{-1} and (ii) 650.1 cm^{-1} (arrows represents vibrations in plane along the tetracene axis) and in rubrene junctions at (iii) 432 cm^{-1} and (iv) 616.4 cm^{-1} (arrows represent vibrations out of plane perpendicular to the tetracene axis). Schematics of the molecular vibration shown here is taken from Ref. 19.

nant states at 100 and 121 mV are observed, suggesting a disordered growth of rubrene films. Based on a previous study on trap-assisted tunneling,[17] the energy level of the trap (V_t) above the electrode Fermi level and the physical position of the trap (d_t) from the bottom electrode are extracted using $V_t = V_r V_f/(V_r + V_f)$ and $d_t = d_o V_f/(V_r + V_f)$, where V_f and V_r are the position of the trap peak in forward and reverse bias, respectively, of the IETS data (reverse bias not shown in the IETS plot for clarity) and d_o is the effective electrical thickness of the barrier. A dielectric constant of 3.0 for rubrene was used in estimating d_o.[18] The calculations for the trap states at 100 mV and 121 mV gave a value of $V_t = 50$ mV, $d_t = 44$ Å and $V_t = 60$ mV, $d_t = 47$ Å, respectively. However, the number of trap states and their corresponding location within the barrier were not the same from sample to sample, suggesting extrinsic origin, due to growth-related structural defects.

In order to understand the difference in the active vibration modes and their relative intensities observed in the two types of junctions, the IETS data were compared with the molecular vibration simulations reported by Weinberg-Wolf *et al.*[14,19] It is known that in IETS, the tunneling electrons interact preferably with the vibrational modes that involve oscillating bond dipoles parallel to the direction of electron flow.[20–22] In HJ, the peak observed at 81 mV, corresponding to an IR mode (650 cm^{-1}), involves oscillations along the tetracene backbone axis of the rubrene molecule. Similarly, the intense active modes at 150 mV (1201 cm^{-1} IR mode) and 165 mV (1331 cm^{-1} Raman mode) also show vibrations along the tetracene backbone axis [see Fig. 1(b) (i and ii)], strongly suggesting azimuthal (vertically up) growth of rubrene molecules on the alumina seed layer. In RJ, however, these modes are absent, whereas other modes at 53 mV (432 cm^{-1} Raman mode), 76 mV (616 cm^{-1} IR mode), and 163 mV (1307 cm^{-1} Raman mode) are observed, which correspond to oscillations transverse to the tetracene backbone axis involving the side rings [see Fig. 1(b) (iii and iv)]. This indicates that in the latter case, the rubrene molecule prefers to grow flat on the electrode resulting in disordered growth of the film. Similar observations of different growth morphologies of OSs are reported by other techniques as well[10,23] and may be attributed to the different electronic coupling of the organic molecules with the growth surface controlled by the surface local density of states.[24]

Higher-energy modes at 177.5 and 193.5 mV were also seen in both the HJ and RJ, corresponding to the vibrational modes in the side phenyl rings of the rubrene molecule. Few low intensity modes with transverse oscillations are also noted in the HJ at 47 mV (377 cm^{-1} IR mode) and 122 mV (978 cm^{-1} IR or Raman mode), which we interpret as arising from the top rubrene-metal interface. In Fig. 1, the IETS data are shown for junctions with Al electrodes since it was found to give less background noise and help comprehend the information contained in these plots better. With ferromagnetic (FM) electrodes [Co and Py (or Fe) as the bottom and top electrodes, respectively], a large nonlinear background was present, which smeared out the peaks at lower bias ($< \sim 70$ mV). However, a systematic and careful study on multiple samples, both with FM and Al electrodes, showed similar activity of the molecular vibrations leading to the same conclusions.

We also investigated the evolution of the growth morphology of rubrene with increasing thickness. For thin films (<10 nm), the IETS results concur with the conclusions from the cross-sectional transmission electron microscope images taken on magnetic tunnel junction structures.[11] It reproducibly showed a considerable dependence of the rubrene film thickness on the growth surface: nearly double the barrier thickness in HJ compared to RJ, for the same nominal rubrene thickness (read from the *in situ* quartz monitor). For thicker films (>10 nm), IETS loses the sensitivity to distinguish between the interface and bulk molecular layers. This is experimentally observed with the presence of additional second-order peaks in the IETS plot. In such cases, we tried to study the evolution of the rubrene morphology using

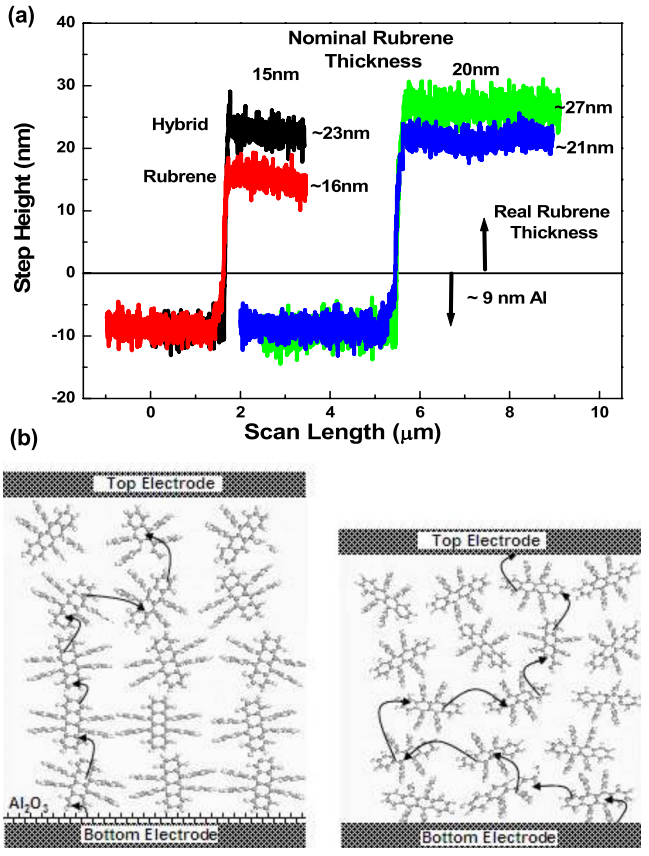

FIG. 2. (Color online) (a) Shows the rubrene film thickness measured using a profilometer for Al(6)/Rub(x)/Al(3) and Al(6)/Al_2O_3(0.7)/Rub(x)/Al(3) with two different values of the nominal thickness: x=15 and 20 nm. (b) Schematics: (Left) azimuthal growh of rubrene molecules on the alumina seed layer in HJ leading to stronger inter-molecular electronic coupling; (Right) disordered nonazimuthal growth of rubrene on metal electrode in RJ leading to a strong hopping dominant transport.

thickness measurement and electrical transport measurements in an attempt to separately probe the bulk and the interface properties. Thickness measurements were performed on thicker rubrene films grown simultaneously on Al and Al_2O_3 surfaces with the same nominal thickness (of 15 and 20 nm), using a profilometer, and is shown in Fig. 2(a). A notable difference in the real thickness of rubrene film for the two types of samples is observed. However, the difference is much less than when the films are thinner.[11] These results imply that molecular ordering is an interface effect driven by the underlying seed layer. With increasing thickness, the bulk disorder smears the preferential azimuthal growth in HJs. Nevertheless, as we will show next, we do observe some remanence of the interface ordering, which affects the transport even at 20-nm-film thickness. Figure 2(b) schematically shows a model for the rubrene layer growth and its effects on the transport properties.

Conductance versus temperature measurements [$G(T)$] were performed for thicker rubrene films and fitted well with existing transport models,[9,25] providing information about the electronic coupling (and hence molecular ordering), both at the injection interface and within the bulk. Figure 3 shows $G(T)$ for the HJ and the RJ at different applied electric field (F) for the nominal rubrene film thickness of 20 nm. It should be noted that the rubrene films were grown simultaneously for HJ and RJ to avoid any growth-related variation for the two cases. The charge injection model developed by Arkhipov *et al.*[9] was used to analyze the results. Here, the injected current is found by considering injection into the Gaussian distribution of states (with variance σ) in the OS followed by either the return of the carrier to the electrode or its diffusive escape into the bulk. The injected current I_{inj} is therefore found as a product of the tunneling probability $\exp(-2\gamma_i x_o)$ (i.e., the probability of the carrier reaching the position x_0 in the first jump) and the escape probability $w_{\text{esc}}(x_0)$ (Ref. 9)

$$I_{inj} \propto \int_a^\infty dx_o \exp(-2\gamma_i x_o) w_{\text{esc}}(x_o) \times \int_{-\infty}^{\infty} dE \ \text{Bol}(E) g[U(x_o) - E],$$

where $x=a(\sim 0.6$ nm) is chosen as the surface of organic film, γ_i is the interface related inverse localization radius and Bol(E) is the Boltzmann factor

$$\text{Bol}(E) = \begin{cases} \exp(-E/k_B T), & E > 0 \\ 1, & E > 0, \end{cases}$$

k_B is the Boltzmann constant

and $U(x)$ is the energy barrier for injection given by $U(x) = \phi - \frac{q^2}{16\pi\varepsilon_o\varepsilon_r x} - qFx$, where ϕ is the energy difference between the Fermi level of the electrode and the highest occupied molecular-orbital level of rubrene, q is the electronic charge, $\varepsilon_o\varepsilon_r$ is the dielectric constant arising due to image forces, and F is the applied electric field. It should be noted that the inverse localization length (γ) contains information about the electronic coupling that can provide structure-related information. Furthermore, they can have different values at the interfaces (γ_i) and within the bulk (γ_b).

The injection model fits our experimental curves in the two junctions with the extracted parameters (ϕ, σ, γ_i) shown in Fig. 3. For the optimized fitting parameters, the model reproducibly matches the experimental curve for different F, supporting the validity of the fits. A large ϕ for RJ (1.03 eV) is inferred compared to HJ (0.49 eV), in agreement with previous studies of thin rubrene barrier tunnel junctions.[11] In addition $\gamma_i^r/\gamma_i^h \sim 10$ (r and h denote RJs and HJs, respectively) suggests the anisotropic tunneling injection efficiencies in the two junctions: better tunneling injection in HJs compared to that in RJs. This may be due to the presence of the alumina tunnel barrier and also due to the azimuthal growth of the rubrene molecules at the interface leading to a better electronic overlap of the rubrene π-electron cloud with the metal. Such effects can be expected to influence spin injection and transport. In our earlier work, related differences were observed in terms of the spin-polarized tunneling and TMR signals.[11]

The injection model begins to deviate at low T and low F. Bulk transport,[25] viz., one-dimensional (1D) hopping

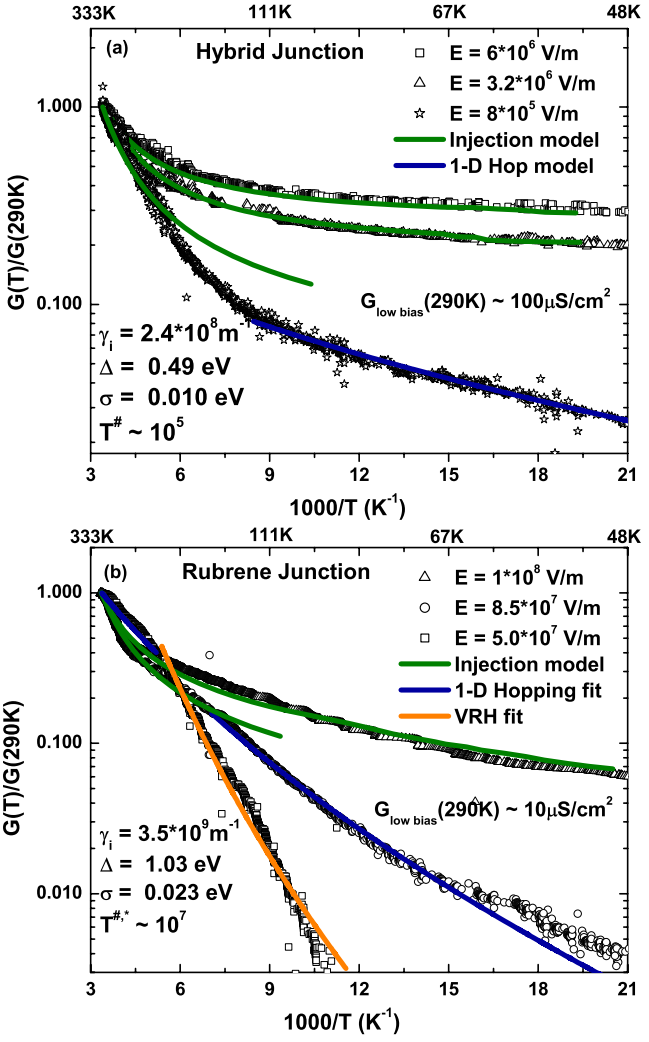

FIG. 3. (Color online) Normalized conductance (log scale) vs inverse temperature plotted in (a) HJ [Co(8)/Al_2O_3(0.6)/Rub(40)/Fe(8)] and (b) RJ [Co(8)/Rub(40)/Fe(8)]. The fit of experimental curves to charge injection and bulk transport models with the extracted parameters are shown.

$\{G(T)\alpha \exp[-(T^{\#}/T)^{-1/2}]\}$ and variable range hopping (VRH) $\{G(T)\alpha \exp[-(T^{*}/T)^{-1/4}]\}$, where $T^{\#,*}\alpha\gamma_b$ (bulk-related inverse localization radius), were instead fitted under these conditions, showing a gradual change from charge injection to the bulk transport-limited regime. At such low bias and temperature, a constant density of states near the Fermi level in the organic film is assumed to contribute to bulk conduction. A change from 1D hopping to VRH hopping was observed in RJ at lower F. In contrast, no sign of such strong temperature dependence of G was noted in HJ. Only at low electric fields ($F < \sim 1 \times 10^6$ V/m) and low temperatures was the 1D hopping model found to fit the curve for HJ. The fit is shown for the lowest measurable value of F (8×10^5 V/m). The relatively stronger temperature dependence of G observed in RJ compared to HJ suggests the highly disordered growth of rubrene molecules (or weaker electronic coupling) in our RJs. This is supported by the inequality $\gamma_b^r > \gamma_b^h(T^{\#,*}\alpha\gamma_b)$ obtained from the parameters $T^{\#,*}$, extracted using bulk models, signifying stronger intermolecular coupling in HJs. These results clearly show that the bottom seed layer (Al_2O_3 in our case) plays an important role for efficient spin injection by influencing the growth of rubrene molecules at the interface. Further, the results suggest some remanence of this ordering into the bulk (up to 20 nm in this case), providing efficient spin transport.

The interface magnetization was probed by PNR measurements using the NG1 reflectometer at NIST. Large area samples ($\sim$1.1 cm^2) with a structure similar to the junctions used for transport studies, with Co and Fe/CoO as the bottom and top layers, were prepared on unetched Si substrates. The nominal thickness of the rubrene film was 10 nm and 20 nm for the hybrid and the rubrene samples, respectively. The samples were cooled down in a magnetic field of 0.7 T to achieve exchange pinning of the Fe layer at the Fe/CoO interface. Using a supermirror polarizer and analyzer, the neutron beam was polarized parallel to the magnetic field, which was applied in the sample plane, as described in Ref. 26. The reflectivity data were corrected for beam footprint, instrument background, and efficiencies of the polarizing elements (typically $>97\%$). Four reflectivity cross sections were measured: $R^{+\,+}$ and R^{--} labeled nonspin flip (NSF) as the neutron retains its original polarization after scattering from the sample, and $R^{+\,-}$ and $R^{-\,+}$, labeled spin flip (SF), where the neutron spin flips it polarization, from the up (+) to down state (−) and vice versa, upon scattering. The nuclear scattering length density (SLD) of a material or chemical SLD (ρ_{chem}) can be determined from fits to the NSF reflectivity data[26–28] in order to extract a profile of the chemical composition of the film as a function of depth. In addition, the vector magnetization of the film as a function of depth can be ascertained from simultaneous fits to the NSF and SF cross sections. Specifically, the splitting between the NSF reflectivity cross sections is sensitive to the component of the magnetization parallel to the applied field. The SF reflectivity is entirely of magnetic origin and is sensitive only to the component of the magnetization perpendicular to the applied field. The NSF PNR data were fit[29] with the REFLPAK (Ref. 30) and GAREFL (Ref. 31) software suites to obtain the chemical and magnetic depth profiles. While spin-flip scattering was measured at all fields considered in this study, the scattering was observed to be negligible (data not shown), indicating no significant moment perpendicular to the applied field.

The reflectivity data collected at 5 K confirmed expectations from SQUID magnetometry that the two FM layer magnetizations are aligned parallel (P) in high fields (H_a =0.7 T) and antiparallel (AP) in low fields (H_a=10 mT). Figure 4 shows the NSF reflectivity measurement ($R++$ and $R--$) for both the rubrene and the hybrid sample at H_a =0.7 T, along with the corresponding depth profile of the nuclear SLD and the layer magnetic moment for the two samples obtained from the fit to the reflectivity data. The most significant difference between the samples includes a lower value of the rubrene nuclear SLD and a larger value of the rubrene layer thickness relative to its nominal value (i.e., $\sim$1.5 times the nominal thickness, compared to 1.1 times) obtained for the hybrid sample relative to the rubrene sample (Fig. 4). This result is in line with the different morphology and packing density of the rubrene molecules (Fig. 2) grown

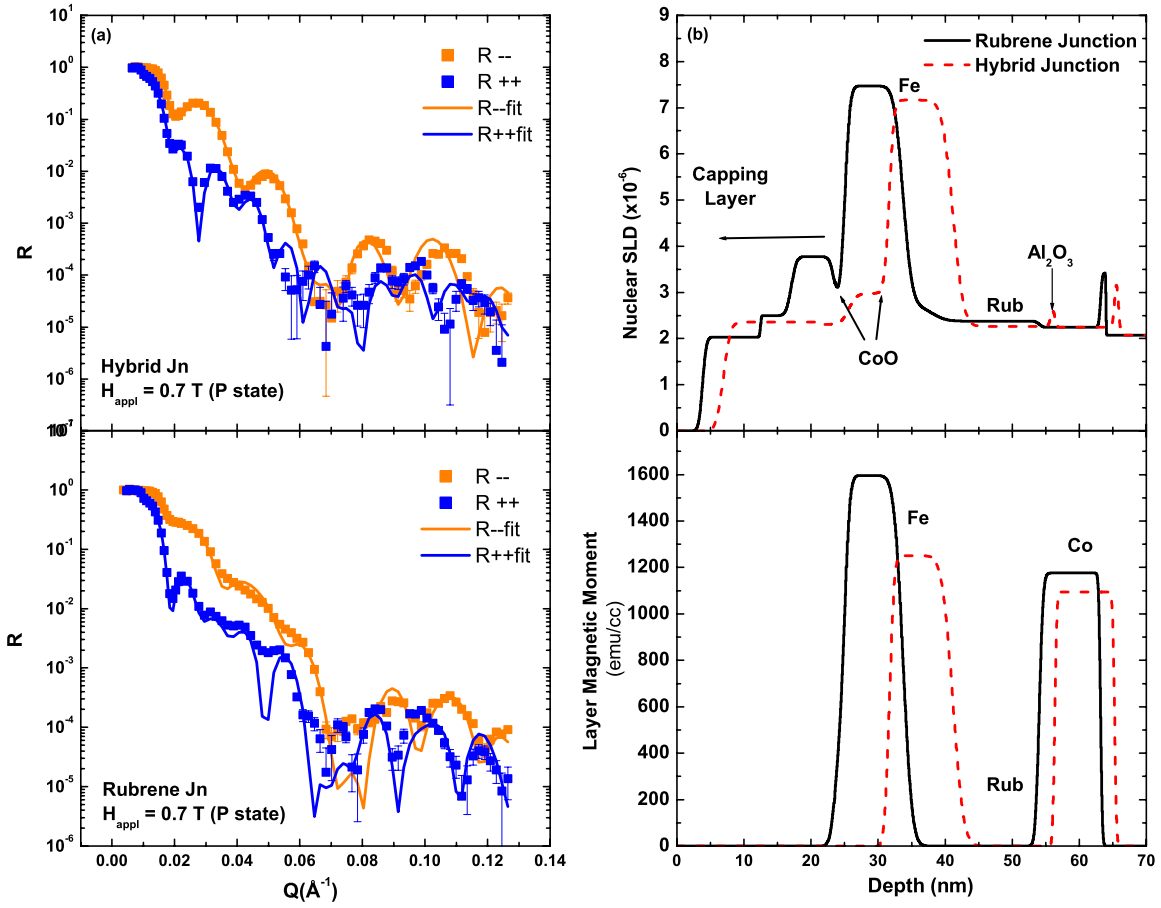

FIG. 4. (Color online) (a) Measured NSF reflectivity data ($R++$ and $R--$) and the corresponding fits for both the hybrid Si/SiO(1)/Co(8)/Al_2O_3(0.6)/Rub(15)/Fe(8)/CoO(1.5) and rubrene: Si/SiO(1)/Co(8)/Rub(20)/Fe(8)/CoO(1.5) samples at H_a=0.7 T. (b) Depth profile of the nuclear SLD (top) and the layer magnetic moment (bottom) obtained from the PNR fits for the hybrid and rubrene samples.

on different seed layers (i.e., Co or Al_2O_3), as described earlier. The structural characteristics of the underlying Co layer in both samples, as determined from PNR, are similar. Specifically, the structural roughness (i.e., corresponding to the width of the interface between the Co layer and the layer above) at the Co/rubrene and Co/Al_2O_3 interfaces in rubrene and hybrid samples, respectively, is comparable in both samples (Fig. 4). Similar magnetic moments (~1100 emu/cc) for the free bottom Co layer were also observed in the P and AP states of the hybrid and the rubrene sample. We thus conclude that there is minimal in-plane magnetic domain formation in the bottom FM electrode in the P and AP states because the structural disorder within the Co layer is limited.

In general, the moments for all the FM layers in both samples were found to be lower than the bulk values (Co-1422 emu/cc and Fe-1700 emu/cc), which is consistent with expectations for fine-grained polycrystalline thin FM layers and more so for the top FM layers with additional interfacial disorder. The average magnetic moment of the top Fe layer in the hybrid sample was considerably lower, by ~20% for both AP and P states, compared to the average Fe moment in the rubrene sample (Fig. 4). This difference although puzzling is an interesting result and requires careful interpretation within the context of the corresponding structural morphology of the upper layers in the two samples. First, it is unlikely that oxidation of the Fe is the source for the reduced moment in the hybrid structure because the samples were well protected with a thick bilayer of Al(7 nm)/Al_2O_3(5 nm) over it (Fig. 4). The nuclear SLD of the CoO layer adjacent to the Fe was found to be lower than the bulk value ($\sim 4.27 \times 10^{-6}$ Å^{-2}) in the hybrid sample, suggesting a reduced structural density of the upper layers rather than enhanced oxidation. Another possibility is that the reduced Fe moment is a direct consequence of higher roughness of the rubrene layer in hybrid structure. However, the PNR fitting analysis showed that the roughness of the rubrene/Fe layer is similar (~3 nm) in the two samples though there exists a higher roughness at the top interface of the Fe layer in the hybrid sample (~1.3 nm) compared to in the rubrene sample (~0.7 nm).

A more significant finding is a lower nuclear SLD for Fe in the hybrid sample (Fig. 4) presumably indicating that the structural density is reduced from that of bulk Fe. A possible origin of this reduction emerges from an understanding of the growth of Fe at the first few layers, which can be directly influenced by the structural properties of the underlying rubrene layer. Given the roughness of the rubrene/Fe interface,

a significant disorder of Fe at this interface (continuing into the bulk) is probable in both samples. In hybrid structures, due to the lower packing density and the azimuthal growth of rubrene molecules, one can expect such disorder to be more pronounced in Fe leading to the reduced SLD. The structural properties of the top Fe electrode in hybrid samples therefore affect its magnetic response showing the reduced moment. Also, they lead to a higher interface roughness of the top Fe layer in the hybrid structure. This is expected to have a direct influence on the exchange coupling and tend to weaken the pinning of the Fe layer. Correspondingly, the magnetic response of Fe at the Fe/rubrene interface can differ from the rest of the layer. This will require a careful and systematic study that will be followed in the future.

The weak exchange pinning due to the rubrene/Fe interface behavior in HJ may lead to random spin fluctuations that are detrimental for spin injection and transport. A way to mitigate this influence was to modify the junction stack. We decided to exchange bias the bottom smooth Co layer and make the top Fe layer free. MR measurements were performed for the HJs with a rubrene thickness of 25 nm (shown in Fig. 5). A MR of 7% was observed at 4.2 K, reducing to ~4.5% at 77 K. No MR was noticed at room temperature. A sharp switching between the P and the AP states are noted, suggesting the advantage of having a strongly exchange pinned Co layer and a free top Fe layer. The gradual decrease in MR with bias at 77 K (see Fig. 5 inset) indicated the good quality of the junctions. Further, we were able to detect spin transport signals through thicker rubrene films (25 nm), a significant improvement in our device performance. In comparison, small (~0.4%) or no MR was measured even in the most stable thin rubrene barrier junctions (5 nm), confirming the strong influence of interface ordering on spin injection.

In conclusion, we have observed the influence of the seed layer on the growth morphology of the rubrene molecules at the interface. Different growth mechanisms lead to a highly anisotropic conduction mechanism that affects both charge and spin injection and transport properties. Although this study reveals better spin transport in molecularly ordered films, PNR result shows a corresponding complex nature of interface magnetic behavior, highlighting the open challenges that have to be carefully addressed and tailored if organic materials are to reach their theoretical expectations in spintronics application.

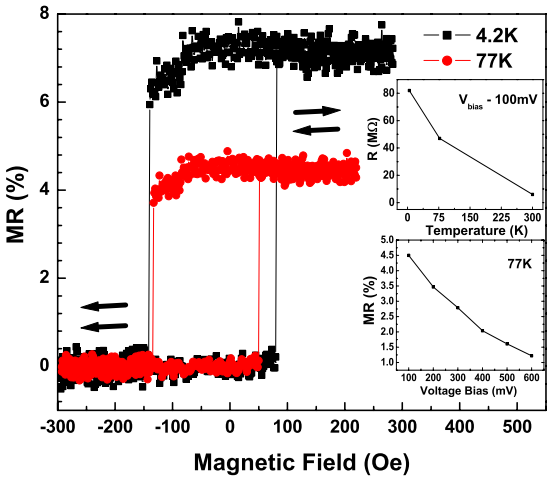

FIG. 5. (Color online) MR measurement (minor loop) performed on HJ: $CoO(1)/Co(8)/Al_2O_3(0.6)/Rub(25)/Fe(12)$ at 77 and 4.2 K. The bottom Co electrode is pinned to the CoO layer by cooling the sample in negative field. Insets: top shows the increase in junction resistance with cool down and the bottom shows the gradual decrease in MR with applied bias at 77 K. The shift in the curve (toward left) is due to a residual current from the power supply, flowing through the magnet.

This work was supported by the KIST-MIT program funds, the ONR Grant No. N00014-09-1-0177, and the NSF Grant No. DMR-0504158.

*vkarthik@mit.edu

[1] W. J. M. Naber, S. Faez, and W. G. van der Wiel, J. Phys. D **40**, R205 (2007).
[2] Z. H. Xiong, Z. Di Wu, Valy Vardeny, and Jing Shi, Nature (London) **427**, 821 (2004).
[3] T. S. Santos, J. S. Lee, P. Migdal, I. C. Lekshmi, B. Satpati, and J. S. Moodera, Phys. Rev. Lett. **98**, 016601 (2007).
[4] V. Dediu, L. E. Hueso, I. Bergenti, A. Riminucci, F. Borgatti, P. Graziosi, C. Newby, F. Casoli, M. P. De Jong, C. Taliani, and Y. Zhan, Phys. Rev. B **78**, 115203 (2008).
[5] V. N. Prigodin, N. P. Raju, K. I. Pokhodnya, J. S. Miller, and A. J. Epstein, Adv. Mater. **14**, 1230 (2002).
[6] Ö. Mermer, G. Veeraraghavan, T. L. Francis, Y. Sheng, D. T. Nguyen, M. Wohlgenannt, A. Köhler, M. K. Al-Suti, and M. S. Khan, Phys. Rev. B **72**, 205202 (2005).
[7] V. Coropceanu, J. Cornil, D. A. da Silvo Filho, Y. Olivier, R. Silbey, and J.-L. Bre'das, Chem. Rev. (Washington, D.C.) **107**, 926 (2007).
[8] M. A. Baldo and S. R. Forrest, Phys. Rev. B **64**, 085201 (2001).
[9] V. I. Arkhipov, E. V. Emelianova, Y. H. Tak, and H. Bässler, J. Appl. Phys. **84**, 848 (1998).
[10] S. C. B. Mannsfeld, A. Virkar, C. Reese, M. F. Toney, and Z. Bao, Adv. Mater. **21**, 2294 (2009).
[11] J. H. Shim, K. V. Raman, Y. J. Park, T. S. Santos, G. X. Miao, B. Satpati, and J. S. Moodera, Phys. Rev. Lett. **100**, 226603 (2008).
[12] R. C. Jaklevic and J. Lambe, Phys. Rev. Lett. **17**, 1139 (1966); J. Lambe and R. C. Jaklevic, Phys. Rev. **165**, 821 (1968).
[13] P. K. Hansma, *Tunneling Spectroscopy: Capabilities, Application and New Techniques* (Plenum Press, New York, 1982).
[14] J. R. Weinberg-Wolf, L. E. McNeil, S. Liu, and C. Kloc, J. Phys.: Condens. Matter **19**, 276204 (2007).
[15] A. L. Geiger, B. S. Chandrashekhar, and J. G. Adler, Phys. Rev. **188**, 1130 (1969).
[16] D. C. Tsui, R. E. Dietz, and L. R. Walker, Phys. Rev. Lett. **27**, 1729 (1971).
[17] M. Wang, W. He, and T. P. Ma, Appl. Phys. Lett. **86**, 192113

(2005).
[18] S. Fratini, H. Xie, I. N. Hulea, S. Ciuchi, and A. F. Morpurgo, New J. Phys. **10**, 033031 (2008).
[19] http://www.physics.unc.edu/project/mcneil/MolecularAnimations/anim.php
[20] J. Kirtley, D. J. Scalapino, and P. K. Hansma, Phys. Rev. B **14**, 3177 (1976).
[21] N. M. D. Brown, R. B. Floyd, and D. G. Walmsley, J. Chem. Soc., Faraday Trans. 2 **75**, 17 (1979); N. M. D. Brown, W. J. Nelson, and D. G. Walmsley, *ibid.* **75**, 32 (1979).
[22] J. T. Hall and P. K. Hansma, Surf. Sci. **77**, 61 (1978).
[23] R. J. Kline, M. D. Mcgehee, and M. F. Toney, Nature Mater. **5**, 222 (2006).
[24] G. E. Thayer, J. T. Sadowski, F. Meyer zu Heringdorf, T. Sakurai, and R. M. Tromp, Phys. Rev. Lett. **95**, 256106 (2005).
[25] N. F. Mott, Philos. Mag. **19**, 835 (1969).
[26] G. P. Felcher, Phys. Rev. B **24**, 1595 (1981).
[27] M. R. Fitzsimmons and C. F. Majrkzak, *Modern Techniques for Characterizing Magnetic Materials* (Kluwer, Norwell, MA, 2005).
[28] K. V. O. Donovan and N. F. Berk, *Neutron Scattering from Magnetic Materials* (Elsevier, Amsterdam, The Netherlands).
[29] C. F. Majkrzak, Physica B **221**, 342 (1996).
[30] P. A. Kienzle, K. V. O'Donovan, J. F. Ankner, N. F. Berk, and C. F. Majkrzak, http://www.ncnr.nist.gov/reflpak (2000–2006).
[31] P. A. Kienzle, M. Doucet, D. J. McGillivray, K. V. O'Donovan, N. F. Berk, and C. F. Majkrzak, http://www.ncnr.nist.gov/reflpak (2000–2006).